Impact of Kinetic Inductance on the Critical-Current Oscillations of Nanobridge SQUIDs

Heleen Dausy,* Lukas Nulens, Bart Raes, Margriet J. Van Bael, and Joris Van de Vondel
Quantum Solid-State Physics, Department of Physics and Astronomy, KU Leuven, Celestijnenlaan 200D, 3001 Leuven, Belgium

(Received 10 March 2021; revised 13 April 2021; accepted 16 June 2021; published 6 August 2021)

In this work, we study the current-phase relation (CΦR) of lithographically fabricated molybdenum germanium ($Mo_{79}Ge_{21}$) nanobridges that is intimately linked with the nanobridge's kinetic inductance. We do this by imbedding the nanobridges in a superconducting quantum interference device (SQUID). We observe that, for temperatures far below T_c, the CΦR is linear, as long as the condensate is not weakened by the presence of a supercurrent. We demonstrate lithographic control over the nanobridge kinetic inductance, which scales with the nanobridge aspect ratio. This allows the $I_c(B)$ characteristic of the SQUID to be tuned. The SQUID properties that can be controlled in this way include the SQUID's sensitivity and the positions of the critical-current maxima. These observations can be of use for the design and operation of future superconducting devices, such as magnetic memories or flux qubits.

DOI: 10.1103/PhysRevApplied.16.024013

I. INTRODUCTION

Superconducting nanobridges with large sheet resistances in the normal state can provide a large kinetic inductance, L_K [1,2]. The large kinetic inductance results from the kinetic energy of the supercurrent charge carriers and, in contrast to the geometric self-inductance, it does not couple with a magnetic field [3]. Moreover, the kinetic inductance is nonlinear with both current and temperature. These unique properties of high-kinetic-inductance nanobridges and nanowires result in their application as scalable key elements in many recently demonstrated device applications, ranging from single-photon detectors [4] to qubit readout and qubit architectures [5–9], magnetic memories and sensors [10,11], and superconductor microwave detectors [12,13]. Despite the technical relevance and many applications of high-kinetic-inductance devices, it is complicated to precisely measure the kinetic inductance value. Existing methods to extract this value either require complex device structures, like resonator circuits, or rely on the total inductance's temperature dependence to separate geometric and kinetic contributions [14–17].

Here, we show a straightforward way to determine the kinetic inductance of a nanobridge. Using this method, we conduct an experimental study of lithographically fabricated $Mo_{79}Ge_{21}$ superconducting nanobridges and their current-phase relation (CΦR). The latter is approximately given by [18–22]

$$I_s = \frac{\Phi_0}{2\pi}\frac{1}{L_K}\varphi. \tag{1}$$

Here, I_s is the supercurrent through the nanobridge; L_K is its kinetic inductance; and φ is the phase difference across the nanobridge, which is limited by a critical value, φ_c, above which the bridge transits to the normal state. We do this by imbedding the nanobridges in a superconducting quantum interference device (SQUID) [21,23–25]. The response of the SQUIDs used in this work is completely determined by their kinetic inductance, making the critical current versus magnetic field oscillations, $I_c(B)$, of the SQUIDs directly reflect the CΦR, and hence, the kinetic inductance of the nanobridge [21,25].

We observe that, for $T \ll T_c$, the CΦR is linear everywhere apart from the region where both SQUID arms near their critical-phase difference. This nonlinearity can be captured by introducing a nonlinear kinetic inductance into Eq. (1), which is quadratic in the current and originates from kinetic suppression of the condensate. We show that, for devices of the same thickness, the L_K values scale with nanobridge dimensions as $\sim L/W$ for the lithographically fabricated nanobridges. Here, L and W are the length and width of the nanobridge, respectively. Furthermore, we demonstrate that the SQUID's $I_c(B)$ characteristic is tunable through lithographic control over the nanobridge dimensions. In this way, SQUID properties, like the SQUID's sensitivity and the positions of the critical-current maxima, can be controlled. These observations are beneficial for future superconducting device

*heleen.dausy@kuleuven.be

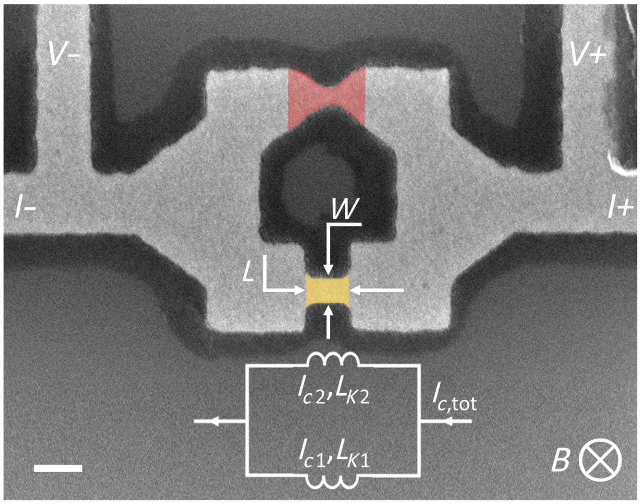

FIG. 1. Scanning-electron-microscopy (SEM) image of a prototypical SQUID device. Area indicated in red corresponds to the Dayem bridge, while the yellow area indicates the nanobridge. Width W and length L of the latter are indicated. White scale bar represents 200 nm. Four-point current and voltage contacts are indicated as $I\pm$ and $V\pm$, respectively. White circuit diagram presents an equivalent electronic circuit of the SQUID. L_{K1} and L_{K2} represent inductances of each branch, while I_{c1} and I_{c2} represent two critical currents of each branch. $I_{c,\mathrm{tot}}$ is the total critical current of the SQUID. Applied magnetic field, B, is oriented as shown.

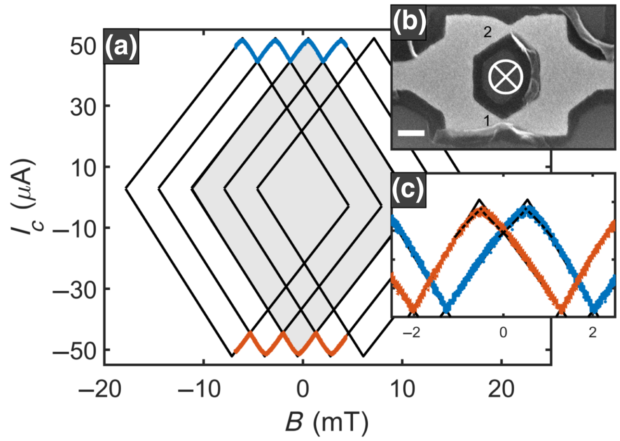

FIG. 2. (a) Critical current versus magnetic field for device g, which contains two Dayem bridges. Measured critical currents for positive (negative) bias are shown in blue (red). Solid lines represent vorticity diamonds generated by the model (see text). Fitting parameters of the vorticity diamonds are $I_{c1} = (27.5 \pm 0.8)$ μA, $\varphi_{c1} = (10.2 \pm 0.1)$ rad, $I_{c2} = (24.7 \pm 0.9)$ μA, $\varphi_{c2} = (11.2 \pm 0.1)$ rad, $L_{K1} = (122 \pm 4)$ pH, and $L_{K2} = (149 \pm 6)$ pH. $n_v = 0$ vorticity diamond is indicated in gray. (b) Scanning-electron-microscopy image of the investigated device, in which the scale bar corresponds to 200 nm. Applied magnetic field, B, is oriented as shown. Bottom SQUID arm corresponds to $j = 1$ in Eq. (2), top SQUID arm to $j = 2$. (c) Magnification of the top (bottom) vertices of the diamonds; positive currents are again shown in blue, absolute values of the negative critical currents in red. Dotted lines show how taking a nonlinear L_K into account can capture the shape of the diamond top.

design and operation (e.g., magnetic memories and qubit readout).

II. NANOBRIDGE SQUIDS

Figure 1 shows a scanning-electron-microscopy image of a prototypical nanobridge SQUID device, which serves as a platform to study the dependence of the nanobridge CΦR on the bridge dimensions. The fabricated structures are (i) SQUIDs containing two Dayem bridges [see Fig. 2(b)] and (ii) SQUIDs containing one Dayem bridge (indicated in red in Fig. 1) and one well-defined nanobridge weak link (indicated in yellow in Fig. 1) of which the dimensions (length L and width W) are varied. The sample geometry is defined using conventional electron beam lithography, followed by pulsed-laser deposition of a $Mo_{79}Ge_{21}$(25 nm)/Au(5 nm) film and a standard lift-off process [26,27]. The gold layer protects the devices from oxidation. The devices all have a similar superconducting-to-normal-state transition temperature of $T_c \sim 6$ K. From measurements of the superconducting-to-normal-state phase boundary on similarly prepared plain films of $Mo_{79}Ge_{21}$/Au, the coherence length can be determined and is given by $\xi(T = 0\ \mathrm{K}) \sim 10$ nm [28].

For nanobridges in the dirty limit and for $T \ll T_c$, the kinetic inductance, L_K, is proportional to $\hbar R_s/(k_B T_c)$, where R_s is the sheet resistance [1,2]. This implies that high kinetic inductances can be achieved using materials with high sheet resistances. Similar to disordered superconductors, such as Nb-Ti-N ($\rho = 170$ $\mu\Omega$ cm) [29], TiN ($\rho = 100$ $\mu\Omega$ cm) [8,30], Nb-N [31], and granular Al [32], the $Mo_{79}Ge_{21}$ structures discussed here have a high estimated resistivity ($\rho = 219$ $\mu\Omega$ cm), leading to a high kinetic inductance [33]. Another advantage of using $Mo_{79}Ge_{21}$ is the fact that it can be fabricated as a thin homogenous amorphous film [34]. For the kinetic inductance to dominate, the loop size should be small to minimize the geometric contribution to the inductance. For the loop size used, the geometric inductance can be estimated as approximately 2 pH [35].

III. PROPERTIES OF A SQUID CONTAINING TWO DAYEM BRIDGES

First, the properties of a SQUID containing two Dayem bridges are examined. This allows us to obtain the properties of the Dayem bridges used in this work [36], which will act as reference junctions to study the properties of nanobridge-type weak links. A representative scanning-electron-microscopy image is shown in Fig. 2(b). Several

SQUID devices of this type are fabricated and characterized. All measured devices exhibit comparable normal-state resistances, from which the resistance of a single Dayem bridge arm can be extracted as $R_{\text{Day,arm}} = (703 \pm 19)\ \Omega$. Despite the small resistance spread of 3%, it is clear from scanning-electron-microscopy imaging and from the spread of the measured device critical currents that the fabrication process results in an unavoidable spread of the Dayem-bridge-junction parameters.

Figure 2(a) shows the measured critical current versus field data, $I_c(B)$, of a prototypical device, device g. The negative current branches, $I_{c^-}(B)$, shown in red, indicate the field dependence of the critical current obtained when sweeping the current from zero (the superconducting state) towards a large negative-bias current that drives the device into the normal state, whereas the positive current branches, $I_{c^+}(B)$, shown in blue, are obtained when sweeping the current from zero towards a large positive-bias current. All measurements are performed at 300 mK. At each magnetic field value, a set of 100 VI measurements in both sweep directions is obtained using a current ramp rate of 3.6 mA/s. For each of these curves, the critical current is then extracted by means of a voltage criterion of 0.5 mV, which is taken just above the noise level. As the transition is very sharp, the obtained critical currents do not depend on the chosen voltage criterion (at least below 2 mV). The critical currents extracted in this way are shown in Fig. 2(a) as small dots. Due to thermal or quantum fluctuations, phase-slip events cause a premature escape from the superconducting state before the depairing current is reached, resulting in a stochastic distribution of the critical current around an average value [37,38].

The shape of the oscillations can be captured by the vorticity diamond model introduced in Ref. [21]. This model describes a SQUID containing two weak links, which both have a linear CΦR:

$$I_j = I_{cj}\frac{\varphi_j}{\varphi_{cj}}, \tag{2}$$

where I_j represents the supercurrent through the j th weak link, with $j = 1, 2$, and where φ_j is the phase difference of the macroscopic wave function taken between the end points of the j th weak link. Furthermore, $I_{cj} \geq 0$ is the critical current and $\varphi_{cj} \geq 0$ is the critical phase difference at which the weak link switches to the dissipative state.

From Eq. (2) and the second Josephson relation [39,40], it is clear that the j th weak link behaves as an inductor with kinetic inductance $L_{Kj} = (\Phi_0/2\pi)(\varphi_{cj}/I_{cj})$, where Φ_0 is the magnetic flux quantum [see Eq. (1) and the electrical model in Fig. 1]. For typical lengths of the Dayem bridges explored in this work (approximately 150 nm), a linear CΦR represents a reasonable approximation in the explored low-temperature range, $T \ll T_c$ [22]. Indeed, by solving the Ginzburg-Landau equations, it is shown that, for nanobridges longer than $3\xi(T)$, the CΦR becomes multivalued and progressively more linear [19,41]. Although the Ginzburg-Landau formalism is strictly valid only close to T_c, an almost linear CΦR is predicted for thin and long wires, even at $T = 0$ K (see Ref. [11] and references therein). The diamond model does not consider any nonlinear dependences of the kinetic inductance on current or temperature and treats the average critical current and the ideal fluctuation-free depairing current as if they are equal.

The total current through the SQUID is given by

$$I = I_{c1}\frac{\varphi_1}{\varphi_{c1}} + I_{c2}\frac{\varphi_2}{\varphi_{c2}}. \tag{3}$$

As the superconducting-order parameter must be single-valued, the total acquired phase difference around the superconducting loop must be an integer multiple of 2π. When applying an external magnetic field, B, perpendicular to the SQUID loop (with the orientation indicated in Fig. 1), the phase differences across each wire and the electrodes must therefore be related by

$$\varphi_1 - \varphi_2 + 2\pi\frac{B}{\Delta B} = 2\pi n_v. \tag{4}$$

Here, ΔB is the Little-Parks oscillation period [42], while n_v is the vorticity or winding number of the loop. Notably, in Eq. (4), it is assumed that any contribution from the geometric inductance of the SQUID to B can be neglected, effectively decoupling Eqs. (3) and (4). Combining these two equations with the requirement that superconductivity should be destroyed if $\text{abs}(\varphi_j) > \varphi_{cj}$ in any of the bridges, one can calculate the total critical current of the SQUID for a given vorticity, n_v, and applied magnetic field, B. The total critical current of the SQUID, $I_c(B, n_v)$, is assumed to be the smallest total applied current at which the current across either wire reaches its critical value.

For each value of n_v, the solution for $I_c(B, n_v)$ forms a so-called vorticity diamond. As illustrated in Fig. 3(a), the magnetic field range and the range of critical currents in which the $n_v = 0$ vorticity state exists (i.e., the vertices of the diamond) are determined by the asymmetry in critical currents $\alpha = (I_{c1} - I_{c2})/I_{c,\text{tot}}$, with $I_{c,\text{tot}} = I_{c1} + I_{c2}$, and the asymmetry in critical phase differences $\gamma = (\varphi_{c1} - \varphi_{c2})/\varphi_{c,\text{tot}}$, with $\varphi_{c,\text{tot}} = \varphi_{c1} + \varphi_{c2}$. The separate influences of varying phase and current asymmetries are shown in Figs. 3(b) and 3(c), respectively. The n_vth vorticity diamond is identical to the $n_v = 0$ diamond shown in Fig. 3(a), but is shifted along the magnetic field axis by $B = n_v\Delta B$. As the vorticity diamond extends over a range of $B = \Delta B\varphi_{c,\text{tot}}/\pi$ in magnetic field, diamonds of adjacent vorticities overlap if $\varphi_{c,\text{tot}} > \pi$ (i.e., twice the critical phase difference of a conventional tunnel junction, $\varphi_{c,\text{tunnel}} = \pi/2$), resulting in a multivalued critical current. An important property of the vorticity diamond is that, on each branch of the vorticity diamond, the phase difference over one arm of the SQUID remains constant, while the phase difference over the other arm varies linearly with the applied magnetic field. Consequently, each branch of the $I_c(B)$ curve immediately reflects the CΦR of one arm of the SQUID [23]. For branches L and R indicated in Fig. 3(a), the magnetic field dependence of the phase differences, φ_j, over the weak links and the field dependence of the critical current, $I_c(B)$, dependence are given by

$$L:\begin{cases}\varphi_1=\varphi_{c1},\\ \varphi_2(B)=\varphi_{c1}+2\pi\frac{B}{\Delta B},\\ I_c(B)=I_{c1}+\left(\frac{1}{L_{K2}}\frac{\Phi_0}{2\pi}\right)\varphi_2,\end{cases}\qquad R:\begin{cases}\varphi_2=\varphi_{c2},\\ \varphi_1(B)=\varphi_{c2}-2\pi\frac{B}{\Delta B},\\ I_c(B)=I_{c2}+\left(\frac{1}{L_{K1}}\frac{\Phi_0}{2\pi}\right)\varphi_1.\end{cases}\tag{5}$$

As the $n_v=0$ vorticity diamond is point symmetric around the origin, similar expressions exist for the corresponding opposite branches. Considering the field and current orientation with respect to the sample surface used in the experiment, the SQUID's transition to the normal state for branch $L(R)$ corresponds with arm $j=1(2)$ reaching its critical current, corresponding with a critical phase difference of $\varphi_1=\varphi_{c1}(\varphi_2=\varphi_{c2})$. As such, branch $L(R)$ reflects the CΦR of arm $j=2(1)$. Equation (5) also shows that the kinetic inductances, L_{Kj}, of the SQUID arm $j=1(2)$ are inversely related to the diamond slope of branch $R(L)$.

In Fig. 2(a), the solid black lines result from a fit of the $I_c(B)$ data to the model described above. It is clear that the model captures the $I_c(B)$ characteristic well. Notably, the kinetic inductances are determined by the slope of the linear part of each branch of the vorticity diamond. The first observation is that, for this symmetrically designed SQUID, the asymmetries in the critical currents ($\alpha=0.06$), the critical phase differences ($\gamma=-0.05$), and the kinetic inductances ($L_{K1}=122$ pH and $L_{K2}=149$ pH) are small. The kinetic inductances are much larger than the geometric contribution to the inductance (~ 2 pH) [35], which is a key assumption in the model used. The critical phase differences of both Dayem bridges are far larger than $\pi/2$: $\varphi_{c1}=10.2$ rad and $\varphi_{c2}=11.2$ rad. This corresponds to the observation that their length exceeds $3\xi\,(T)$. As introduced in Sec. II, the $I_c(B)$ dependence of each branch of the vorticity diamond is in one-to-one correspondence with the CΦR of the corresponding Dayem bridge. The majority of the experimental data are well captured by the linear edges of the vorticity diamond, implying that the CΦR of the Dayem bridges is indeed approximately linear. However, close to the maximum critical current or maximum critical phase difference [i.e., top and bottom vertices of the vorticity diamond, see Fig. 2(c)], the critical current deviates from a linear dependence on the applied magnetic field for both branches. This reflects that the CΦR is nonlinear over this current range. The nonlinear dependence can be described by introducing a nonlinear kinetic inductance and can be attributed to kinetic suppression of the condensate due to the presence of a supercurrent [43]. For $T\ll T_c$, the kinetic inductance of a superconducting strip can be expanded in terms of the depairing current, $I_{\mathrm{dep}}(B)$, as

$$L_K\left(I_{\mathrm{dep}}\right)=L_K\left(0\right)\left[1+\frac{I_{\mathrm{dep}}^2}{I_*^2}+\cdots\right],\tag{6}$$

where I_* is a constant that sets the scale of the quadratic nonlinearity [12]. No odd-ordered terms appear due to symmetry considerations, as the bridge must have the same kinetic inductance, regardless of the current orientation. Within the Usadel framework, Ref. [43] provides an estimate for the magnitude of the quadratic nonlinearity of $I_*=4.7I_{\mathrm{dep}}/\sqrt{1.9}$, indicating that the nonlinearity becomes important only at currents close to the depairing current of the strip. In Ref. [10], this nonlinearity of the kinetic inductance was exploited to fabricate an ultrasensitive magnetometer.

To summarize, the vorticity diamond's branches directly reflect the bridge CΦRs; the vertices are determined by the asymmetries in critical currents, α, and critical phases, γ; and the nonlinearity at the top vertex is understood to be caused by depletion of the superconducting condensate. In the next section, this approach is used to explore the impact of geometry on the CΦR of the fabricated nanobridges.

IV. PROPERTIES OF SQUIDs CONTAINING ONE DAYEM BRIDGE AND ONE NANOBRIDGE

This section examines the properties of fabricated SQUIDs containing one Dayem bridge and one nanobridge (see Fig. 1), upon changing the nanobridge dimensions, (L,W). The different dimensions, as measured by scanning-electron-beam microscopy, are shown in Table I. The total normal-state resistance of each device, together with the average value of the resistance of a SQUID arm containing a Dayem bridge, allows us to determine the resistance of the SQUID arm containing the nanobridge for each device. These resistance values are consistent with the nanobridge geometries. Figure 4(a) shows the critical current versus field data, $I_c(B)$, for a particular SQUID device (device u), which contains one Dayem bridge and one long nanobridge ($L\sim 319$ nm), as can be seen in Fig. 4(b). The measurement method is the same as that for device g, with a current ramp rate of 3.5 mA/s. For the typical lengths of nanobridges and temperatures explored in this work ($L\sim 100$–340 nm $\gg 3\xi$, $T=300$ mK $\ll T_c$), it is expected that the CΦR of the nanobridge will be quasilinear [11,19,41]. The resulting fit using the model described in Sec. III is shown using solid black lines. It is clear

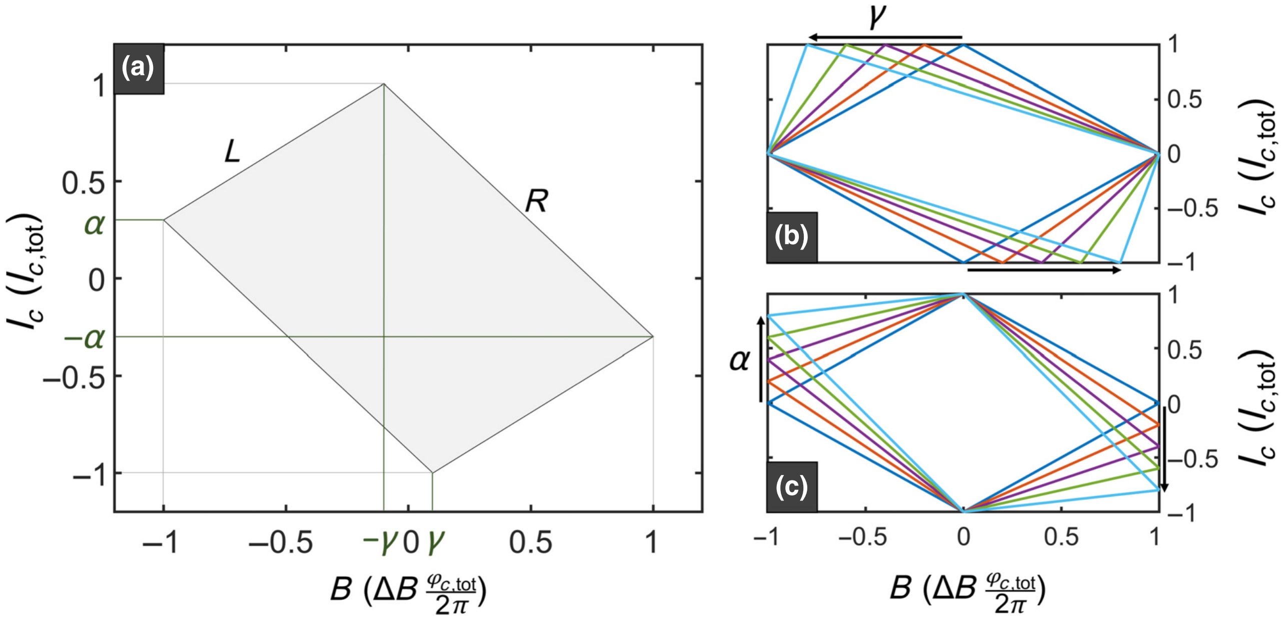

FIG. 3. (a) The $n_v = 0$ vorticity diamond for current-asymmetry $\alpha = 0.3$ and phase-asymmetry $\gamma = 0.1$. Vertices of the diamonds are determined by asymmetries in the critical currents and critical phase differences. The diamond extends over a range $B = \Delta B\varphi_{c,\mathrm{tot}}/\pi$ in magnetic field. The n_vth vorticity diamond is identical to the $n_v = 0$ diamond, but shifted along the magnetic field axis by $B = n_v\Delta B$. (b) Evolution of the diamond shape for $\alpha = 0$ and increasing γ from 0 to 0.8 in steps of 0.2, as indicated by the arrows. (c) Evolution of the diamond shape for $\gamma = 0$ and for increasing α from 0 to 0.8 in steps of 0.2, as indicated by the arrows.

that once again, the model captures the $I_c(B)$ characteristic well.

As introduced in Sec. III, the $I_c(B)$ dependence of each branch of the vorticity diamond is in one-to-one correspondence with the CΦR of the corresponding Dayem or nanobridge. Similarly to the Dayem bridges in Sec. III, the experimental data are well captured by the linear edges of the vorticity diamond. This reflects that the CΦR of the nanobridge is approximately linear. Only close to the maximum critical current or maximum critical phase difference [i.e., top vertices of the vorticity diamonds, see Fig. 4(c)] is the CΦR nonlinear. This can be captured by introducing a nonlinear inductance into Eq. (5) [see dotted line in Fig. 4(c)]. The kinetic inductances obtained from the fitting ($L_{K1} = 261$ pH and $L_{K2} = 156$ pH) are substantially larger than the geometric contribution to the inductance (~ 2 pH) [35]. Since the kinetic inductance scales with the length and width of the bridge as $L_K \sim L/W$, the kinetic inductance of the nanobridge, L_{K1}, is about 65% larger than the kinetic inductance of the Dayem bridge, L_{K2}. This difference is reflected in the different slopes ($\sim 1/L_K$) of the branches of the vorticity diamond. The critical phase differences of both the Dayem bridge ($L \sim 150$ nm) and nanobridge are far larger than $\pi/2$. The critical phase difference for a nanowire can be estimated to be [11]

$$\varphi_{c,\mathrm{est}} \sim (\pi/2)(L/2\xi), \tag{7}$$

and scales with the length of the bridge. This is in correspondence with the observation that the critical phase difference of the nanobridge ($\varphi_{c1} = 13.5$ rad) is about 70% larger than that of the Dayem bridge ($\varphi_{c2} = 7.9$ rad), which has a smaller effective length. However, for the nanobridge of device u, which has a length $L \sim 319$ nm, this estimate provides $\varphi_{c,\mathrm{est}} \sim 25$ rad, which exceeds the value obtained from the fitting procedure. Notably, this estimate is an overestimate, as premature switching due to thermal and quantum fluctuations does not allow the maximum fluctuation-free depairing current and corresponding critical phase difference to be reached [44] (see Sec. V). For device u, the depairing current can be estimated as $I_{\mathrm{dep}} = 2.6k_BT_c/eR_\xi = 52\ \mu$A, where R_ξ is the resistance of a length of wire equal to ξ [44]. This value exceeds the experimentally measured critical current. The device incorporates both a Dayem bridge and nanobridge, which have different CΦRs. This results in different kinetic inductances (slopes of the diamonds). The asymmetry in critical currents ($\alpha = 0.01$) remains small, but there is a strong asymmetry in critical phase differences ($\gamma = 0.26$). The latter relocates the top and bottom vertices of the vorticity diamond [see Figs. 3(b) and 3(c)]. More specifically, the top of the $n_v = 0$ diamond (indicated in gray) is clearly shifted from the $B = 0$ mT axis towards negative field values.

Several SQUIDs containing one Dayem bridge and one nanobridge (see Fig. 1) are investigated, upon changing the dimensions (L, W) of the nanobridge. Figure 5(a) shows

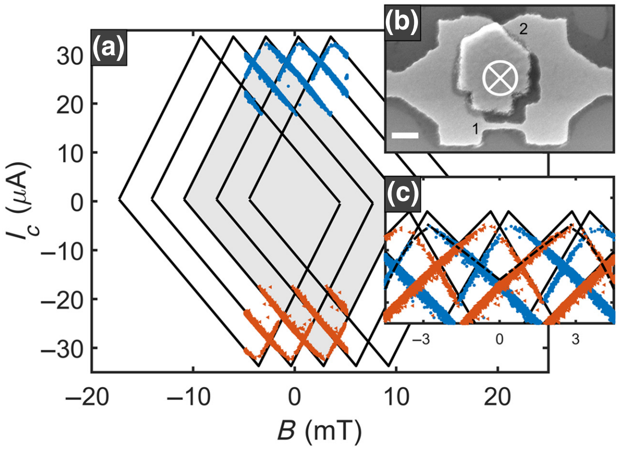

FIG. 4. (a) Critical current versus magnetic field for device u, which contains a nanobridge of length $L \sim 319$ nm and width $W \sim 34$ nm. Measured critical currents for positive (negative) bias are shown in blue (red). Solid lines represent vorticity diamonds generated by the model. Fitting parameters of the vorticity diamonds are $I_{c1} = (17.1 \pm 0.8)$ μA, $\varphi_{c1} = (13.5 \pm 0.6)$ rad, $I_{c2} = (16.7 \pm 0.6)$ μA, $\varphi_{c2} = (7.9 \pm 0.6)$ rad, $L_{K1} = (261 \pm 17)$ pH, and $L_{K2} = (156 \pm 15)$ pH. $n_v = 0$ vorticity diamond is indicated in gray. (b) Scanning-electron-microscopy image of the investigated device; scale bar corresponds to 200 nm. Applied magnetic field, B, is oriented as shown. Bottom SQUID arm corresponds to $j = 1$ in Eq. (2), top SQUID arm to $j = 2$. Due to incomplete lift-off, the inner part of the SQUID is not completely removed. (c) Magnification of the top (bottom) vertices of the diamonds; positive currents are again shown in blue, the absolute values of negative critical currents in red. Dotted lines show how taking a nonlinear L_K into account can capture the shape of the diamond top.

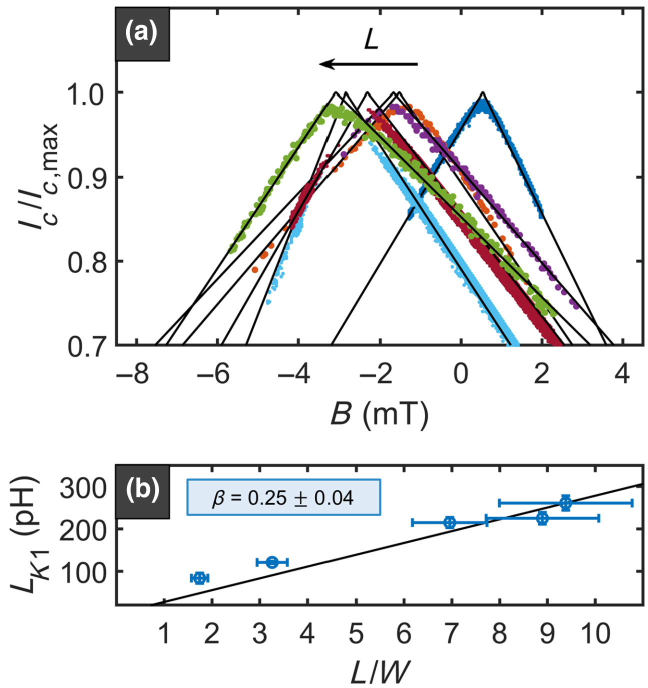

FIG. 5. (a) Field dependence of the current-normalized $n_v = 0$ vorticity diamond for devices g (blue), c (red), m (purple), u (light blue), v (burgundy), and w (green). Arrow at the top shows the increase in the nanobridge length L. (b) Kinetic inductance of the nanobridges, as obtained from the fitting procedure, versus aspect ratio of the bridge for devices c, m, u, v, and w. Solid line shows linear fitting, using $L_K = \beta(L/W)(\hbar R_s/k_B T_c)$, where $T_c = 6$ K and $R_s = 88$ Ω. Fitting yields $\beta = 0.25 \pm 0.04$.

experimental data corresponding to the $n_v = 0$ vorticity diamond for different devices and fitting using the model in Sec. III. To compare different devices, critical currents are normalized to the top of their fitted vorticity diamonds, $I_c^*(B) = I_c(B)/I_{c,\max}$. Notably, to obtain critical-current values in a particular field range, data obtained using different measurement protocols are merged (see Appendix). The estimated dimensions of the nanobridge from scanning-electron-beam microscopy and the fitting parameters obtained using the model from Sec. III are shown in Table I.

It is clear that the slopes of the vorticity diamonds change upon changing the nanobridge dimensions. In Fig. 5(b), the dependence of the nanobridge kinetic inductance on the nanobridge aspect ratio, L/W, is shown, together with the fitting result using the theoretical expectation for kinetic inductance of a nanobridge [12]:

$$L_K = \beta \frac{L}{W} \frac{\hbar R_s}{k_B T_c}. \tag{8}$$

TABLE I. Nanobridge dimensions (length L and with W) are listed, together with fitting parameters of each device: each SQUID arm is described by its critical current, I_{cj}; critical phase difference, φ_{cj}; and the linear part of its inductance, L_{Kj}. Device g consists of two Dayem bridges, so no nanobridge dimensions are given.

Device	L (nm)	W (nm)	I_{c1} (μA)	I_{c2} (μA)	φ_{c1} (rad)	φ_{c2} (rad)	L_{K1} (pH)	L_{K2} (pH)
g			27.5 ± 0.8	24.7 ± 0.9	10.2 ± 0.8	11.2 ± 0.1	122 ± 4	149 ± 6
c	101 ± 5	58 ± 5	58 ± 3	39 ± 4	15 ± 2	12 ± 2	84 ± 12	105 ± 21
m	176 ± 5	54 ± 5	49.9 ± 0.9	39 ± 1	18.4 ± 0.2	15.4 ± 0.2	121 ± 3	131 ± 4
u	319 ± 5	34 ± 5	17.1 ± 0.8	16.7 ± 0.9	13.5 ± 0.6	7.9 ± 0.6	261 ± 17	156 ± 15
v	313 ± 5	45 ± 5	23.3 ± 0.8	23 ± 1	15.2 ± 0.7	10.9 ± 0.7	215 ± 12	158 ± 14
w	338 ± 5	38 ± 5	28 ± 1	29 ± 1	19 ± 1	13 ± 1	225 ± 14	147 ± 13

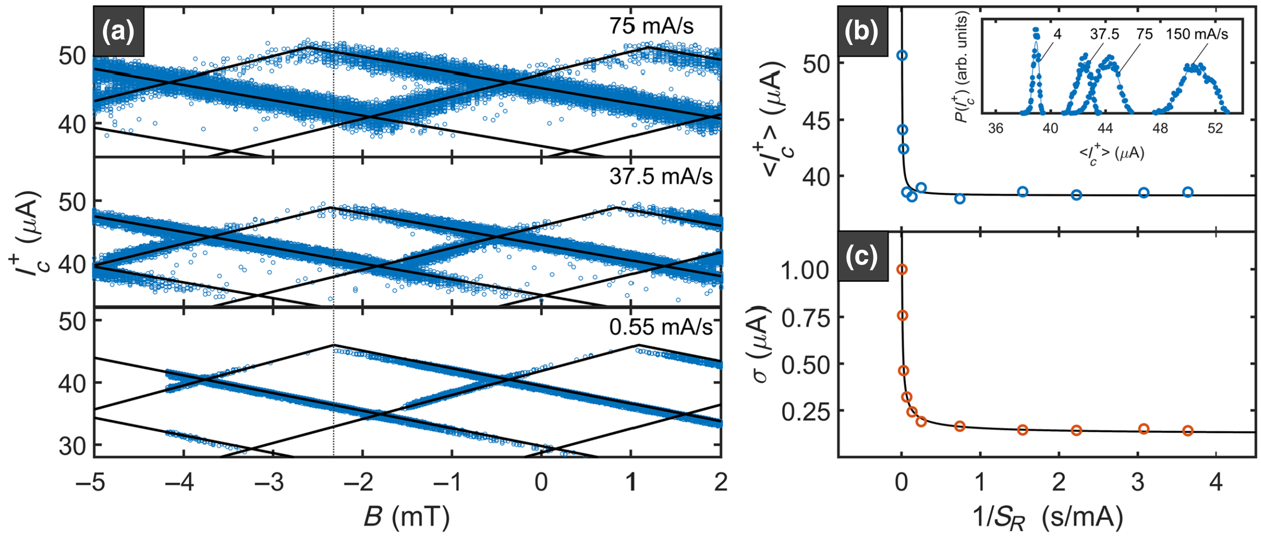

FIG. 6. (a) $I_c^+(B)$ characteristics of device v, shown for different sweep rates (0.55, 37.5, and 75 mA/s). Gray dotted line shows that the current-maximum position is only impacted by high sweep rates. (b) Dependence of the average nanobridge positive critical current on sweep rate (S_R) for device v at $B = 0$ mT, with sweep rates ranging from 0.275 to 150 mA/s. Inset shows the stochastic distribution for selected sweep rate values. (c) Dependence of the standard deviation of the nanobridge positive critical current on sweep rate for device v at $B = 0$ mT, with sweep rates ranging from 0.275 to 150 mA/s. At least 2500 critical currents per field value are collected to calculate the average critical current and its standard deviation. Above this value, both the average and standard deviation converge towards an asymptotic value for all sweep rates.

Here, T_c is approximately 6 K and the sheet resistance, R_s, is estimated to be 88 Ω. From fitting, one obtains $\beta = 0.25 \pm 0.04$, whereas within the Ginzburg-Landau framework, theory suggests $\beta \sim 0.14$–0.18 [12,44]. This indicates that the nanobridge kinetic inductance, and hence, the diamond slope (and thus, SQUID sensitivity), can be controlled by means of the bridge dimensions. In comparison with the lift-off procedure used to fabricate the samples in this work, a fabrication process that relies on etching could be beneficial to reduce the variation of device characteristics. Notably, the sheet resistance is inversely proportional to the device thickness. The devices studied here have a relatively large thickness, but it is possible to grow homogeneous Mo-Ge films as thin as 1 nm [45,46], thereby providing an easy way to increase the kinetic inductance even more.

Moreover, the position of the maximum critical current position shifts to more negative field values compared with device g, which corresponds to a larger difference in critical phase differences, $\varphi_{c1} - \varphi_{c2}$. In particular, it shifts to the left for increasing nanobridge lengths [see Fig. 5(a) and Eq. (7)]. It is not straightforward to quantitatively compare the critical phase differences and currents obtained from the fitting procedure (see Table I), as some of the critical currents are obtained using a different current sweep rate. As thoroughly discussed in Ref. [47], high current sweep rates have an effect on the maximum attainable critical current and corresponding critical phase difference. This effect is negligible for the sweep rates used in this section, as demonstrated in Sec. V.

V. INFLUENCE OF SWEEP RATE

Figure 6(a) shows the critical current, $I_c^+(B)$, of one specific device (device v) for three different sweep rates (0.55, 37.5, and 75 mA/s). The right side of the figure shows the average value, $\langle I_c^+ \rangle$ [Fig. 6(b)], and standard deviation, σ [Fig. 6(c)], of the critical current at one specific field value ($B = 0$ mT), which corresponds to probing the nanobridge. The inset of Fig. 6(b) shows the stochastic distribution for selected sweep rate values (4, 37.5, 75, and 150 mA/s).

It is clear that the maximum attainable critical current increases for the highest sweep rates. This can be explained as follows: due to thermal and quantum fluctuations of the superconducting phase (called phase slips), the sample transits to the normal state before reaching the maximum pair-breaking current [37,48]. In the ideal fluctuation-free case, φ_c in Eq. (1) is determined by the condition where I_s reaches the depairing current limit. As such, the measured CΦR, which is sensitive to fluctuations, only reflects part of the ideal fluctuation-free CΦR. If one could sweep infinitely fast, the timescales of these fluctuations would be too large to have an effect and the critical current would be equal to the depairing current. This means that, by using higher sweep rates, it is possible to better approach the ideal CΦR [47]. For this device, the depairing current can be roughly estimated to be $I_{\text{dep}} \approx 60$ μA [44], which agrees with the data shown in Fig. 6(b). Figure 6(c) illustrates that the standard deviation of the critical-current distribution also increases for increasing sweep rates. This could indicate that fewer consecutive phase-slip events are needed to switch to the normal state for high sweep rates (i.e., higher average critical current), which is directly linked to the stronger thermal footprint of a phase-slip event at higher currents (i.e., higher average critical current) [48–51].

Figure 6(a) shows that the shift of the vorticity diamond top is only pronounced at higher sweep rates and very small between 0.55 and 37.5 mA/s. The data shown in Fig. 5(a) are obtained with maximum sweep rates of 4 mA/s, that is, in a regime where the influence of the sweep rate is negligible, making quantitative comparison between different devices possible. Notably, the diamond slope, and thus, the kinetic inductance, is insensitive to the current sweep rate.

VI. CONCLUSION

Here, we study $Mo_{79}Ge_{21}$ superconducting nanobridges and their CΦR by imbedding them in a SQUID. The response of these SQUIDs is completely determined by their high kinetic inductance, L_K, making the critical current versus magnetic field oscillations, $I_c(B)$, of the SQUIDs directly reflect the CΦR of the nanobridge. For $T \ll T_c$, the CΦR is linear everywhere apart from close to the critical phase difference. This nonlinearity can be understood as kinetic suppression of the condensate. We demonstrate that the SQUID's $I_c(B)$ characteristic is tunable through lithographic control over the nanobridge dimensions. L_K scales linearly with the nanobridge aspect ratio, L/W. This tunability and magnitude of L_K, together with its nonlinearity, make our $Mo_{79}Ge_{21}$ nanobridges extremely suitable for many applications, ranging from magnetic memories [11] to microwave detectors [12,13]. Furthermore, the measured L_K can be maximized further by limiting the device thickness. This opens up the possibility to use the $Mo_{79}Ge_{21}$ nanobridges as phase-slip centers for phase-slip flux qubits [44].

ACKNOWLEDGMENTS

This work is supported by the Research Foundation-Flanders (FWO, Belgium), Grant No. G0B5315N, as well as by the COST action NanoCoHybri (CA16218).

APPENDIX: MEASUREMENT PROTOCOLS

All measurements are performed at 300 mK in an Oxford Instruments Heliox VL ^{3}He cryostat. During these measurements, a room-temperature π filter with a cutoff frequency of 1 MHz is consistently used.

Flux oscillations are measured using a standard four-probe technique, using different protocols. We obtain $I_c(B)$ data by performing a standard *VI* measurement at a particular B value. This method only reveals part of the $I_c(B)$ curves, sometimes resulting in only a few data points for one particular branch. This makes it complex to perform an accurate fitting. To solve this problem and to generate more data points along each branch, a preparation protocol based on that introduced in Ref. [11] is employed. In this procedure, the concept of a "unique vorticity diamond" is exploited. In the unique vorticity diamond, shown as a gray shaded region in Fig. 7, there is only one stable vorticity state.

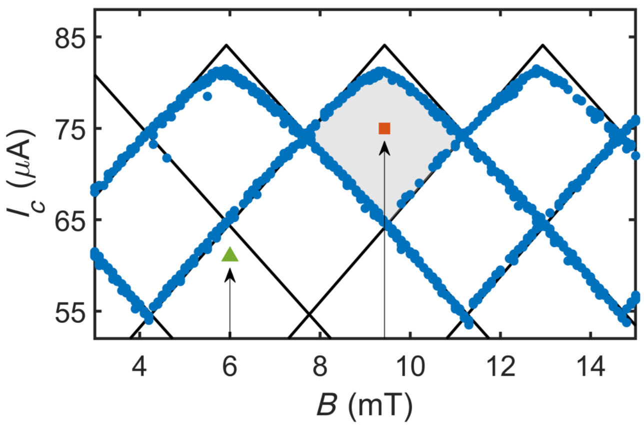

FIG. 7. Positive flux oscillations, $I_c^+(B)$, of a $Mo_{79}Ge_{21}$ nanobridge SQUID. Unique vorticity diamond of $n_v = 3$ is indicated by the gray area. System is prepared in the $n_v = 3$ vorticity state by repeatedly applying a bias current in the unique vorticity diamond, as indicated by the red square. After that, the field is changed to the readout value under zero bias current. Once there, the critical current is measured by taking a regular *VI*, as shown by the green triangle. By repeating this process, both branches of the diamond can be probed. Same procedure is applicable to the other vorticity diamonds.

To prepare the system in a specific vorticity state, we can apply an external magnetic field corresponding to the unique vorticity-diamond field range. Then, we repeatedly apply a bias current, which leads to switching to the normal states for all vorticity states, except for the one associated with the unique vorticity diamond (shown by the red square). Once prepared, the system is driven to the readout field value under zero bias. When the readout value is reached, the critical current is measured through a regular *VI* (indicated by the green triangle). This allows us to probe a larger part of each vorticity diamond.

To generate more I_c values at every field value, we use the setup shown in Fig. 8. This setup allows us to collect many *VI* curves in a short period of time. For this, a triangular ac current wave signal is applied using a function generator (Keithley K6221). The current-bias amplitude and frequency can be controlled, resulting in a controllable current sweep rate. The sample response is acquired via a low-noise preamplifier (Stanford Research Systems SR560), after which the amplified signal passes to a digital phosphor oscilloscope (Tektronix TDS5032B). LabView software was developed to automatically extract the switching current from the collected *VI* values using a

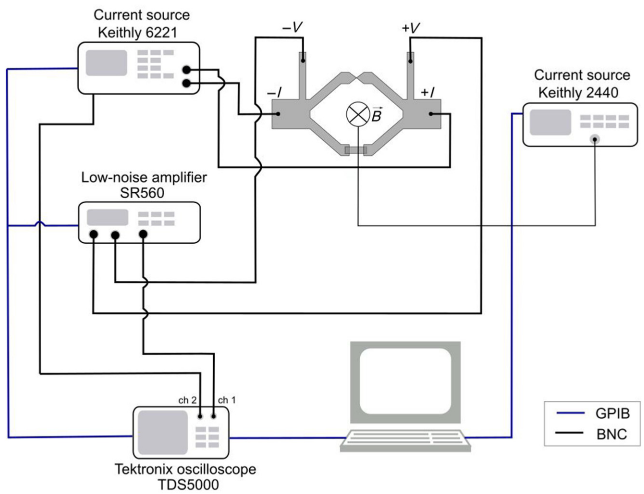

FIG. 8. Schematic overview of the ac setup.

voltage criterion. The field is controlled through a current (supplied by a Keithley K2400 instrument) pushed through superconducting magnetic coils.

[1] M. Tinkham, *Introduction to Superconductivity* (McGraw-Hill Book Co., New York, 1996), 2nd ed.

[2] A. J. Annunziata, D. F. Santavicca, L. Frunzio, G. Catelani, M. J. Rooks, A. Frydman, and D. E. Prober, Tunable superconducting nanoinductors, Nanotechnology **21**, 445202 (2010).

[3] A. N. McCaughan, Q. Zhao, and K. K. Berggren, nanoSQUID operation using kinetic rather than magnetic induction, Sci. Rep. **6**, 28095 (2016).

[4] P. K. Day, H. G. LeDuc, L. Frunzio, G. Catelani, M. J. Rooks, A. Frydman, D. E. Prober, B. A. Mazin, A. Vayonakis, and J. Zmuidzinas, A broadband superconducting detector suitable for use in large arrays, Nature **425**, 817 (2003).

[5] J. E. Mooij, T. P. Orlando, L. L. Levitov, L. Tian, C. H. van der Wal, and S. Lloyd, Josephson persistent-current qubit, Science **285**, 1036 (1999).

[6] V. E. Manucharyan, J. Koch, L. I. Glazman, and M. H. Devoret, Fluxonium: Single Cooper-pair circuit free of charge offsets, Science **326**, 113 (2009).

[7] B. H. Eom, P. K. Day, H. G. LeDuc, and J. Zmuidzinas, A wideband, low-noise superconducting amplifier with high dynamic range, Nat. Phys. **8**, 623 (2012).

[8] J. T. Peltonen, P. C. J. J. Coumou, Z. H. Peng, T. M. Klapwijk, J. S. Tsai, and O. V. Astafiev, Hybrid rf SQUID qubit based on high kinetic inductance, Sci. Rep. **8**, 10033 (2018).

[9] Y. Schön, J. N. Voss, M. Wildermuth, A. Schneider, S. T. Skacel, M. P. Weides, J. H. Cole, H. Rotzinger, and A. V. Ustinov, Rabi oscillations in a superconducting nanowire circuit, npj Quantum Mater. **5**, 18 (2020).

[10] J. Luomahaara, V. Vesterinen, L. Grönberg, and J. Hassel, Kinetic inductance magnetometer, Nat. Commun. **5**, 4872 (2014).

[11] A. Murphy, D. V. Averin, and A. Bezryadin, Nanoscale superconducting memory based on the kinetic inductance of asymmetric nanowire loops, New J. Phys. **19**, 063015 (2017).

[12] J. Zmuidzinas, Superconducting microresonators: Physics, and applications, Annu. Rev. Condens. Matter Phys. **3**, 169 (2012).

[13] G. Coiffard, M. Daal, N. Zobrist, N. Swimmer, S. Steiger, B. Bumble, and B. A. Mazin, Characterization of sputtered hafnium thin films for high quality factor microwave kinetic inductance detectors, Supercond. Sci. Technol. **33**, 07LT02 (2020).

[14] R. Meservey and P. M. Tedrow, Measurements of the kinetic inductance of superconducting linear structures, J. Appl. Phys. **40**, 2028 (1969).

[15] Y. Shimazu and T. Yokoyama, Measurement of kinetic inductance of superconducting wires, and application for measuring flux state of Josephson-junction loops, Physica C **412–414**, 1451 (2004).

[16] H. Wang, R. Yang, G. Li, L. Wu, X. Liu, L. Chen, J. Ren, and Z. Wang, Inductance analysis of superconducting quantum interference devices with 3D nano-bridge junctions, Supercond. Sci. Technol. **31**, 055015 (2018).

[17] H. Cai, H. Li, E. Y. Cho, and S. A. Cybart, Inductance of $YBa_2Cu_3O_{7-\delta}$ thin-films with, and without superconducting ground planes, IEEE Trans. Appl. Supercond. **30**, 7500205 (2020).

[18] K. K. Likarev, Superconducting weak links, Rev. Mod. Phys. **51**, 101 (1979).

[19] K. Hasselbach, D. Mailly, and J. R. Kirtley, Micro-superconducting quantum interference device characteristics, J. Appl. Phys. **91**, 4432 (2002).

[20] D. Hazra, J. R. Kirtley, and K. Hasselbach, Nano-superconducting quantum interference devices with continuous read out at milliKelvin temperatures, Appl. Phys. Lett. **103**, 093109 (2013).

[21] A. Murphy and A. Bezryadin, Asymmetric nanowire SQUID: Linear current-phase relation, stochastic switching, and symmetries, Phys. Rev. B **98**, 094507 (2017).

[22] D. Hazra, Nanobridge superconducting quantum interference devices: Beyond the Josephson limit, Phys. Rev. B **99**, 144505 (2019).

[23] M. L. Della Rocca, M. Chauvin, B. Huard, H. Pothier, D. Esteve, and C. Urbina, Measurement of the Current-Phase Relation of Superconducting Atomic Contacts, Phys. Rev. Lett. **99**, 127005 (2007).

[24] A. A. Burlakov, V. L. Gurtovoi, A. I. Il'in, A. V. Nikulov, and V. A. Tulin, Superconducting quantum interference device without Josephson junctions, JETP Lett. **99**, 169 (2014).

[25] S. Collienne, B. Raes, W. Keijers, J. Linek, D. Koelle, R. Kleiner, R. B. G. Kramer, J. Van de Vondel, and A. V. Silhanek, Nb-Based Nanoscale Superconducting Quantum Interference Devices Tuned by Eletroannealing, Phys. Rev. Appl. **15**, 034016 (2021).

[26] M. Timmermans, L. Serrier-Garcia, M. Perini, J. Van de Vondel, and V. V. Moshchalkov, Direct observation of condensate, and vortex confinement in nanostructured superconductors, Phys. Rev. B **93**, 054514 (2016).

[27] R. Panghotra, M. Timmermans, C. Xue, B. Raes, V. V. Moschalkov, and J. Van de Vondel, Exploring

the impact of core expansion on the vortex distribution in superconducting-normal-metal hybrid nanostructures, Phys. Rev. B **100**, 054519 (2019).
[28] M. Motta, F. Colauto, J. I. Vestgarden, J. Fritzsche, M. Timmermans, J. Cuppens, C. Attanasio, C. Cirillo, V. V. Moshchalkov, J. Van de Vondel, T. H. Johansen, W. A. Ortiz, and A. V. Silhanek, Controllable morphology of flux avalanches in microstructured superconductors, Phys. Rev. B **89**, 134508 (2014).
[29] T. M. Hazard, A. Gyenis, A. Di Paolo, A. T. Asfaw, S. A. Lyon, A. Blais, and A. A. Houck, Nanowire Superinductance Fluxonium Qubit, Phys. Rev. Lett. **122**, 010504 (2019).
[30] A. Shearrow, G. Koolstra, S. J. Whiteley, N. Earnest, P. S. Barry, F. J. Heremans, D. D. Awschalom, E. Shirokoff, and D. I. Schuster, Atomic layer deposition of titanium nitride for quantum circuits, Appl. Phys. Lett. **113**, 212601 (2018).
[31] D. Niepce, J. Burnett, and J. Bylander, High Kinetic Inductance NbN Nanowire Superinductors, Phys. Rev. Appl. **11**, 044014 (2019).
[32] H. Rotzinger, S. T. Skacel, M. Pfirrmann, J. N. Voss, J. Münzberg, S. Probst, P. Bushev, M. P. Weides, A. V. Ustinov, and J. E. Mooij, Aluminium-oxide wires for superconducting high kinetic inductance circuits, Supercond. Sci. Technol. **30**, 025002 (2017).
[33] H. Tashiro, J. M. Graybeal, D. B. Tanner, E. J. Nicol, J. P. Carbotte, and G. L. Carr, Unusual thickness dependence of the superconducting transition of α-MoGe thin films, Phys. Rev. B **78**, 014509 (2008).
[34] A. Bezryadin, C. N. Lau, and M. Tinkham, Quantum suppression of superconductivity in ultrathin nanowires, Adv. Phys. **404**, 971 (2000).
[35] H. M. Greenhouse, Design of planar rectangular microelectronic inductors, IEEE Trans. Parts Hybrids Packag. **10**, 101 (1974).
[36] P. W. Anderson and A. H. Dayem, Radio-Frequency Effects in Superconducting Thin Film Bridges, Phys. Rev. Lett. **13**, 195 (1964).
[37] M. Sahu, M.-H. Bae, A. Rogachev, D. Pekker, T.-C. Wei, N. Shah, P. M. Goldbart, and A. Bezryadin, Individual topological tunnelling events of a quantum field probed through their macroscopic consequences, Nat. Phys. **5**, 503 (2009).
[38] T. Aref, A. Levchenko, V. Vakaryuk, and A. Bezryadin, Quantitative analysis of quantum phase slips in superconducting $Mo_{76}Ge_{24}$ nanowires revealed by switching-current statistics, Phys. Rev. B **86**, 024507 (2012).
[39] B. D. Josephson, Possible new effects in superconductive tunnelling, Phys. Lett. **1**, 251 (1962).
[40] B. D. Josephson, Supercurrents through barriers, Adv. Phys. **14**, 419 (1965).
[41] G. J. Podd, G. D. Hutchinson, D. A. Williams, and D. G. Hasko, Micro-SQUIDs with controllable asymmetry via hot-phonon controlled junctions, Phys. Rev. B **75**, 134501 (2007).
[42] D. S. Hopkins, D. Pekker, P. M. Goldbart, and A. Bezryadin, Quantum interference device made by DNA templating of superconducting nanowires, Science **308**, 5729 (2005).
[43] A. Anthore, H. Pothier, and D. Esteve, Density of States in a Superconductor Carrying a Supercurrent, Phys. Rev. Lett. **90**, 127001 (2003).
[44] J. E. Mooij and C. J. P. M. Harmans, Phase-slip flux qubits, New J. Phys. **7**, 219 (2005).
[45] J. M Graybeal and M. R. Beasley, Localization, and interaction effects in ultrathin amorphous superconducting films, Phys. Rev. B **29**, 4167 (1984).
[46] C. N. Lau, N. Markovic, M. Bockrath, A. Bezryadin, and M. Tinkham, Quantum Phase Slips in Superconducting Nanowires, Phys. Rev. Lett. **87**, 217003 (2001).
[47] A. Bezryadin and P. M. Goldbart, Superconducting nanowires fabricated using molecular templates, Adv. Mater. **22**, 1111 (2010).
[48] X. D. A. Baumans, V. S. Zharinov, E. Raymenants, S. Blanco Alvarez, J. E. Scheerder, J. Brisbois, D. Massarotti, R. Caruso, F. Tafuri, E. Janssens, V. V. Moshchalkov, J. Van de Vondel, and A. V. Silhanek, Statistics of localized phase slips in tunable width planar point contacts, Sci. Rep. **7**, 44569 (2017).
[49] M. Tinkham, J. U. Free, C. N. Lau, and N. Markovic, Hysteretic I-V curves of superconducting nanowires, Phys. Rev. B **68**, 134515 (2003).
[50] N. Shah, D. Pekker, and P. M. Goldbart, Inherent Stochasticity of Superconductor-Resistor Switching Behavior in Nanowires, Phys. Rev. Lett. **101**, 207001 (2008).
[51] D. Pekker, N. Shah, M. Sahu, A. Bezryadin, and P. M. Goldbart, Stochastic dynamics of phase-slip trains, and superconductive resistive switching in current-biased nanowires, Phys. Rev. B **80**, 214525 (2009).